ACS OMEGA

Open Access

http://pubs.acs.org/journal/acsodf

Article

Oxidation of Gasoline Direct Injection Engine Soot in Oxygen-Lean and Oxygen-Rich Atmospheres: A Comparative Analysis of Physicochemical Properties

Chenxi Wang, Xiangyu Dong, Ye Liu, Xuyang Zhang, Gang lv, and Chonglin Song*

Cite This: *ACS Omega* 2025, 10, 50986−50994

Read Online

ACCESS | Metrics & More | Article Recommendations

ABSTRACT: For most of the time, soot oxidation in gasoline particulate filters (GPFs) occurs in oxygen-lean and high-temperature environments due to the typically stoichiometric combustion mode of gasoline direct injection (GDI). The oxygen-lean and high-temperature atmospheres inevitably change the oxidation characteristics, altering the physicochemical properties of GDI soot particles and consequently affecting the control strategies of GPF regeneration. To gain deeper insight into the GDI soot oxidation process, a detailed investigation into the changes in the physicochemical properties of GDI soot under different oxygen concentrations was performed. The morphology, nanostructure, surface functional group, and hybridized carbon state of the soot samples were analyzed using high-resolution transmission electron microscopy (TEM), X-ray photoelectron spectroscopy (XPS), and Fourier transform infrared spectroscopy (FT-IR). The macroscopic morphology results show that, with the conversion level increased to 80%, both GS-20 and GS-1 soot particles become more compact. The fractal dimension (D_f) of GS-20 and GS-1 soot particles increased by 19.5 and 26.4%, respectively, while their primary particle sizes decreased by 27.4 and 25.5%. Simultaneously, the radius of gyration (R_g) was reduced by 38.2 and 43.4%, respectively. A comparison between the two soot samples indicates that the oxygen-lean atmosphere tends to yield soot with a smaller R_g, a larger primary particle size, and D_f than the oxygen-rich atmosphere, thereby making the subsequent oxidation of GS-1 soot more challenging. From the nanostructural perspective, both soot samples undergo a gradual transformation into a more ordered structure, as evidenced by a similar decrease in fringe tortuosity ($\overline{T_f}$) and an increase in fringe length ($\overline{L_f}$). However, at the same conversion level, GS-1 soot demonstrates a shorter $\overline{L_f}$ and higher $\overline{T_f}$ compared to GS-20, which facilitates oxygen penetration into the primary particles and thus accelerates oxidation. Chemical analysis further reveals that under oxygen-rich conditions, the preferential oxidation of sp^3-hybridized carbon leads to a lower sp^2/sp^3 ratio in GS-1 soot compared to GS-20 at the same level of carbon conversion. In contrast, under oxygen-lean conditions, the relatively limited availability of oxygen leads to a surface concentration of C−OH groups on GS-1 soot that is up to 9.3% lower and C═O groups up to 13.8% lower than those on GS-20 at 80% conversion.

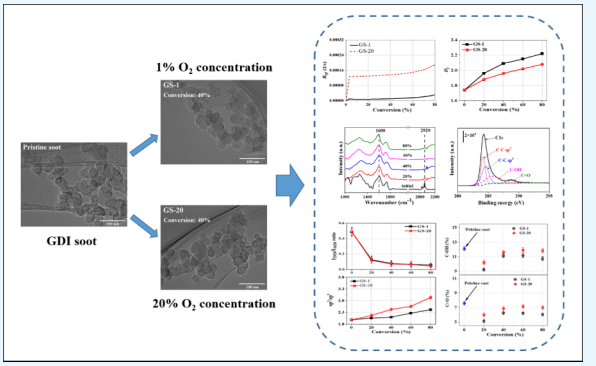

1. INTRODUCTION

At present, gasoline particulate filters (GPFs) are widely used in the after-treatment system of gasoline direct injection (GDI) engines to satisfy increasingly stringent particle emission regulations. With the help of GPFs, the soot emission from GDI engines can be significantly reduced. However, throughout the engine operation, the GPF must be regenerated by removing accumulated soot particles via an oxidation reaction.[1−4] Otherwise, the accumulated soot particles can result in an unacceptable back pressure that lowers fuel economy and even damages the GPFs.[5] Therefore, soot oxidation is crucial for the practical application of GPFs.

There has been considerable interest in the investigation of the physicochemical properties of soot particles during oxidation because these properties not only govern soot oxidative reactivity but also offer additional information concerning the oxidation reaction.[6−12] Numerous studies have reported that the physicochemical properties of soot particles significantly changed with oxidation. For example, Song et al.[13] explored the structure of the biodiesel soot and the Fischer−Tropsch diesel soot during oxidation at 500 °C in air. They found that the oxidation induced a structural

Received: May 23, 2025
Revised: September 14, 2025
Accepted: October 7, 2025
Published: October 21, 2025

transformation for both soot samples, shifting from an amorphous structure toward a more ordered structure. In addition, the biodiesel soot exhibited a hollow capsule structure with long and straight outer graphene layers after internal burning occurred. Setiabudi et al.[14] investigated the roles of NO_2 and O_2 in the soot oxidation reaction. During oxidation, a large number of oxygenated functional groups were created as intermediates on the surface of diesel soot samples and were eventually converted to CO and/or CO_2. To date, such studies have focused almost entirely on diesel soot, with only minimal work regarding GDI soot. Compared with diesel soot, GDI soot tends to comprise smaller primary particles having less-ordered nanostructure and higher metal content.[15,16] Thus, GDI soot is more reactive and more readily oxidized than diesel soot,[15] and thus probably has physicochemical properties different from those of diesel soot during oxidation.

It is well-known that the lean-burn mode of diesel engines yields a high O_2 concentration in the exhaust stream, meaning that diesel soot oxidation occurs in an oxygen-rich environment. In contrast, GDI soot experiences an oxygen-rich oxidation process only when the fuel cut during deceleration is performed to achieve a complete regeneration of the GPF.[17,18] In the case that the engine is operated normally, GDI soot oxidation in the GPF occurs under an oxygen-lean atmosphere because GDI engines normally employ a stoichiometric combustion mode.[17,18] To gain deeper insight into the GDI soot oxidation process, a detailed investigation into the change in the physicochemical properties of GDI soot during oxidation was performed in the present study. Due to the low exhaust soot emission level of GDI engines, it is expensive and time-consuming to harvest a sufficient quantity of exhaust soot. Our previous work[19] confirmed that a commercial carbon black (Special Black 4, Orion Ltd.) has very similar physicochemical characteristics to those of actual GDI soot. Thus, we employed Special Black 4 to represent GDI soot. More details on the similarities between Special Black 4 and GDI soot are provided in ref 19. Oxidation reaction was conducted under both oxygen-lean and oxygen-rich conditions. The physicochemical properties of this GDI soot surrogate, including morphology, nanostructure, surface functional group, and ratio of sp^2 to sp^3 hybridized carbon atoms, were characterized and discussed in detail herein.

2. EXPERIMENTAL SECTION

2.1. Oxidation Reactor. The oxidation process of the soot samples was investigated using a thermogravimetric analyzer (TGA/DSC1) provided by Mettler-Toledo Ltd. In a prior study of Jang et al.,[20] the average exhaust temperatures obtained from a GDI vehicle were found to be 498.7 °C for the FTP-75 drive cycle and 524.4 °C for the WLTC drive cycle. Based on these experimental results, the oxidation tests in the present work were conducted under isothermal conditions of 500 °C at atmospheric pressure. For GDI engines, the O_2 concentration in the exhaust stream is generally in the range of 0.5−1.5% under normal operating conditions, while it can be as high as 20% through the fuel cut in the deceleration to achieve a complete regeneration of GPFs.[21] Thus, two O_2 concentrations were employed for Special Black 4 oxidation: (1) 1% of the O_2 concentration, representative of the normal operating conditions, and (2) 20% of the O_2 concentration, representative of the full regeneration event. The balance gas was ultrapurity N_2, and the total flow rate of feed gas was set at 50 mL/min. For convenience, the Special Black 4 samples oxidized at 1% and 20% O_2 concentrations are denoted thereafter as GS-1 soot and GS-20 soot, respectively.

2.2. Soot Characterization. *2.2.1. High-Resolution Transmission Electron Microscopy (HRTEM).* The soot structure was assessed using a high-resolution transmission electron microscope (FEI Talos F200X) of Thermo Fisher Scientific Ltd. The instrument was operated in the TEM and HRTEM modes to obtain 40,000 and 500,000× magnification images, respectively. The TEM and HRTEM images were subject to the determination of the soot morphology and nanostructure parameters, respectively. The morphology parameters included the primary particle size (d_p), gyration radius (R_g), and fractal dimension (D_f). The nanostructural parameters included the mean fringe length ($\overline{L_f}$) and mean fringe tortuosity ($\overline{T_f}$), where the $\overline{L_f}$ was obtained by measuring the physical length of each fringe based on a pixel size and the $\overline{T_f}$ was the ratio between the $\overline{L_f}$ and the straight-line distance between the two endpoints of the fringe. An image processing software was used to extract the nanostructure parameters of soot samples. The extraction program involves normalization of the HRTEM image, selection of the interest region, binarization, skeletonization, and quantitative calculation of nanostructure parameters. Further details about the analysis procedures are described in ref 22.

2.2.2. Fourier Transform Infrared Spectroscopy. The C−H groups on the soot surface were determined using a Fourier transform infrared spectrometer (FT-IR, Nicolet Nexus 470). In the test, potassium bromide (KBr) pellet pressing was employed as the primary sample preparation method. First, soot particle samples and KBr powder were dried in a vacuum oven for 24 h to minimize moisture-induced −OH absorption. The dried KBr powder was then ground in an agate mortar for 15 min to reduce its particle size to below 2.5 μm, thereby minimizing light scattering effects. The finely ground pure KBr powder was pressed into transparent pellets approximately 0.5 mm thick, which served as the background reference. For the soot samples under investigation, the dried soot particles were mixed with KBr at a mass ratio of 1:50 and further ground for 15 min to ensure uniform dispersion. The resulting mixture was then pressed into pellets for FT-IR measurements. Each sample was measured three times to ensure the reliability and reproducibility of the results. The instrument operated at a scanning resolution of 1 cm^{-1}, covering a spectral range of 1000−3200 cm^{-1}. Each spectrum was processed using background subtraction, baseline correction, and smoothing with the OMNIC software package (Thermo Nicolet).

2.2.3. X-ray Photoelectron Spectroscopy. X-ray photoelectron spectroscopy (XPS, PHI-1600 ESCA) with a Mg-Kα source was employed in this study to investigate the oxygenated functional groups and the hybridized carbon states of soot samples. Before spectral data analysis, the measured binding energies were calibrated using the C 1s peak of the contaminant carbon (binding energy 284.6 eV) as a reference.

3. RESULTS AND DISCUSSION

3.1. Soot Oxidation Evaluation. The isothermal oxidation of the soot samples was performed under the conditions described in Section 2. Each trial was repeated three times, and variations in the results were found to be less than 3%. The mass loss against oxidation time is plotted in Figure 1 for the GS-1 and GS-20 soot samples. Because the GS-20 soot

https://doi.org/10.1021/acsomega.5c04848
ACS Omega 2025, 10, 50986−50994

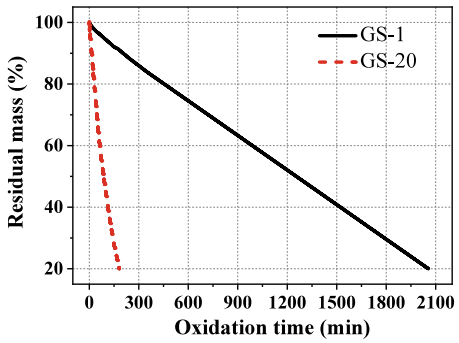

Figure 1. Mass loss as a function of the oxidation time for the GS-1 and GS-20 soot samples.

is processed at a higher O_2 concentration, it has a much shorter oxidation time than the GS-1 soot. As an example, the time spans from initiation of the oxidation to 50% mass loss are 86.7 min for the GS-20 soot and 1255.0 min for the GS-1 soot. According to the proposal of Al-Qurashi and Boehman,[6] the specific oxidation rate (R_{sp}) is calculated as

$$R_{sp} = \frac{dm}{dt}\frac{1}{m_{residue}} \tag{1}$$

where dm/dt is the derivative of soot mass concerning time and $m_{residue}$ is the mass of the unreacted soot. Figure 2 presents

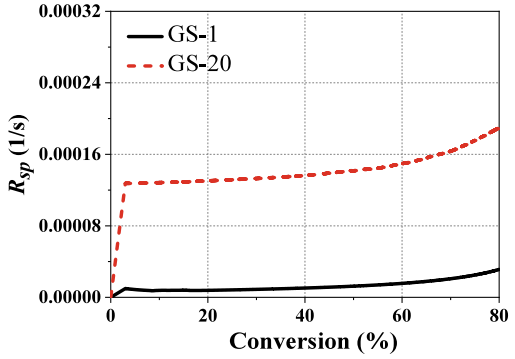

Figure 2. Specific oxidation rates (R_{sp}) of the soot samples at different conversion levels.

the R_{sp} values for the GS-1 and GS-20 soot samples at various conversion (i.e., mass loss) levels. At the same conversion level, the R_{sp} values for the GS-20 soot are 5−15 times larger than those for the GS-1 soot. Given that soot oxidation can affect its physicochemical properties,[6,8−10,15] such a significant difference in R_{sp} raises a question of whether there are also differences in soot characteristics. The subsequent sections shed light on the similarities and differences in the physicochemical properties of the two soot samples during oxidation.

3.2. Soot Morphology. Typical morphology images of the pristine soot and the partially oxidized soot samples are provided in Figure 3. These images demonstrate that both soot samples consist of numerous near-spherical primary particles that aggregate into clusters with irregular geometries. For the soot samples, the d_p, R_g, and D_f values were obtained through analysis of the TEM images. D_f represents the degree of compactness of soot aggregates; a high D_f value is associated with a more compact structure of the soot aggregates.[23] R_g can be used to quantify the size of soot aggregates; a large R_g value indicates larger aggregates.[24]

The d_p, R_g, and D_f values were calculated according to refs 25 and 26. R_g can be obtained via the equation:

$$R_g^2 = \frac{1}{n}\sum_{i=1}^{n} r_i^2 \tag{2}$$

where r_i represents the distance from the center of each primary soot particle within an aggregate to the aggregate's centroid, while n represents the total number of primary soot particles comprising the soot aggregate. The latter is defined as

$$n = (A_a/A_p)^{\alpha} \tag{3}$$

where A_a represents the projected area of the aggregate, while A_p is the projected area of primary particle. An empirical constant of $\alpha = 1.09$ was applied in this equation.[24] D_f is expressed as follows:

$$n = k_f(2R_g/d_p)^{D_f} \tag{4}$$

where k_f is a prefactor. After taking the natural logarithm of eq 4, D_f is determined from the slope of the linear regression plot of the scatter plot generated from ln (n) versus ln ($2R_g/d_p$). Additional details regarding the calculation procedures of d_p, R_g, and D_f are available in refs 25 and 26.

To ensure statistically reliable results, around 100 aggregates with distinct boundaries were selected from each soot sample for the calculation of d_p, R_g, and D_f. Figure 4 shows the d_p distribution histograms with the probability density function of both the GS-1 and GS-20 soot samples at various conversion levels. Overall, both samples exhibit a unimodal and approximately Gaussian distribution at each oxidation stage, indicating relatively homogeneous particle formation and oxidation behavior. At the initial stage (20% conversion), the two samples show similar distributions, with mean particle sizes centered around 27−30 nm. As the conversion increased,

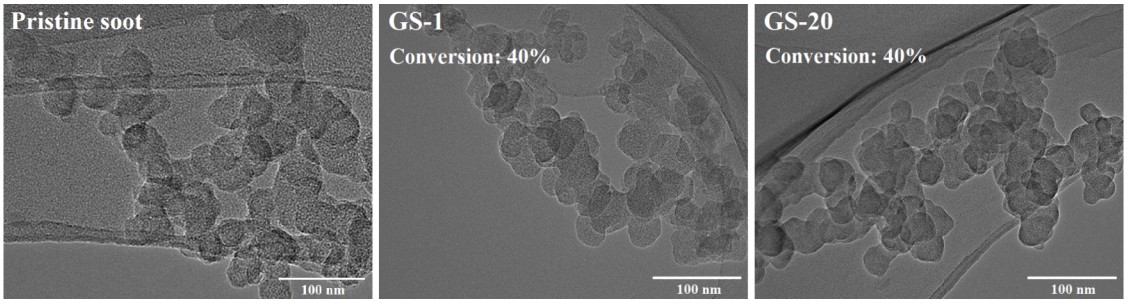

Figure 3. Typical TEM images of pristine soot and soot samples during oxidation.

https://doi.org/10.1021/acsomega.5c04848
ACS Omega 2025, 10, 50986−50994

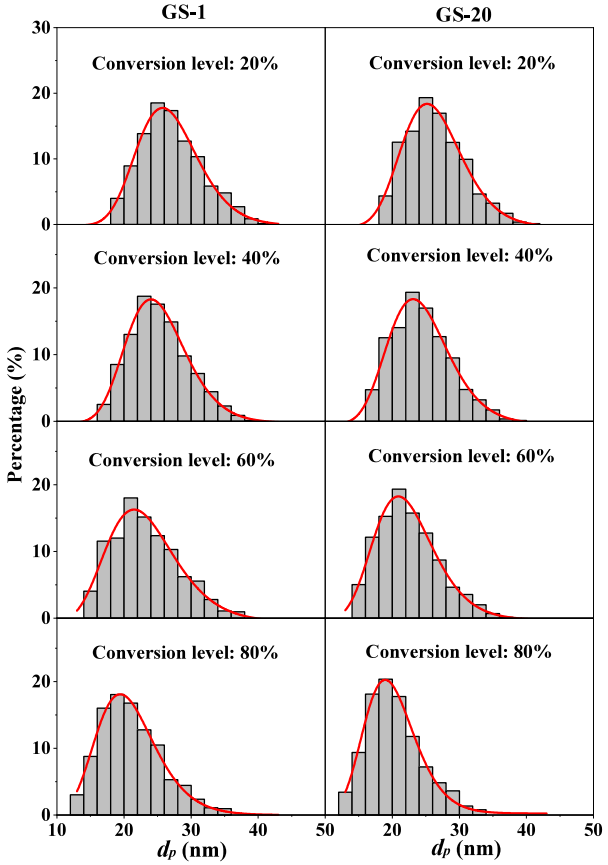

Figure 4. Distributions of the primary particle size (d_p) for the soot samples during oxidation.

a gradual decrease in particle size distribution was observed in both samples, reflecting the progressive consumption of carbonaceous material. Notably, GS-20 exhibits a more symmetric and narrower distribution than GS-1 at higher conversion levels (60 and 80%), suggesting a more uniform oxidation process. In contrast, GS-1 shows broader distributions with more pronounced left-skewness, implying greater heterogeneity in the oxidation rates among particles. The averaged d_p values ($\overline{d_p}$) at various conversion levels are summarized in Figure 5. The $\overline{d_p}$ values gradually decrease from 28.28 to 20.52 nm (27.4% decrease) for the GS-20 soot and from 28.28 to 21.07 nm (25.5% decrease) for the GS-1 soot as oxidation progresses. It is accepted that the soot oxidation

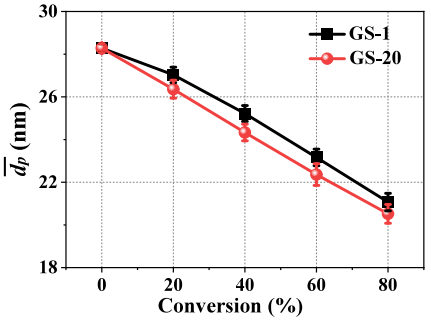

Figure 5. Averaged primary particle sizes ($\overline{d_p}$) at different conversion levels.

follows two modes: internal burning and external burning.[6,13,27] Previous studies[6,13,28,29] have evidenced that internal burning results in a certain number of soot particles with hollow interiors. In this study, however, the hollow structure cannot be observed in all of the HRTEM images, meaning that the soot oxidation likely undergoes the external burning mode. The process of external burning inevitably leads to a gradual decrease in the primary particle size, as indicated in Figure 5. In addition, the $\overline{d_p}$ for the GS-1 soot is slightly larger than that for the GS-20 soot at the same conversion level, which suggests that at lower O_2 concentrations, the external oxidation rate decreases. The soot with larger $\overline{d_p}$ generally has a smaller specific surface area compared to a smaller one, offering fewer active sites and thereby hindering subsequent oxidation.[9,30]

Figure 6 shows the R_g distributions of the soot samples at different conversion levels. Both GS-1 and GS-20 show right-

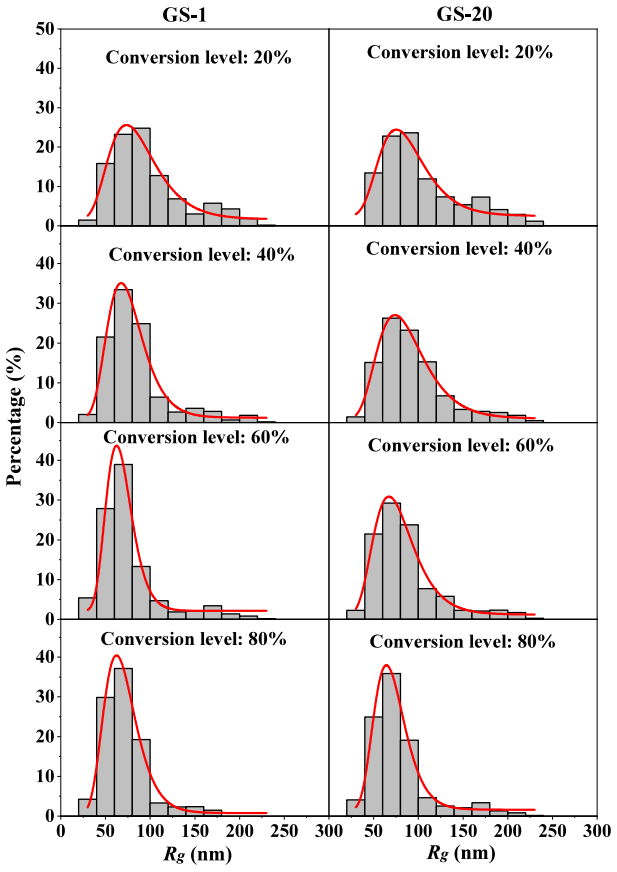

Figure 6. Distributions of the gyration radius values (R_g) for the soot samples during oxidation.

skewed, unimodal R_g distributions at each oxidation stage, with most aggregates falling below 150 nm. A clear trend of decreasing average R_g is observed with increasing conversion for both samples, indicating aggregate shrinkage due to oxidation. For GS-1 soot particles, the shift in the R_g distribution toward smaller values is more pronounced, especially from 20 to 60% conversion. The averaged R_g values ($\overline{R_g}$) during oxidation are plotted in Figure 7. Similar to the $\overline{d_p}$ data in Figure 5, the $\overline{R_g}$ shows a decrease with conversion, from 127.42 to 78.71 nm for the GS-20 soot and from 127.42 to 72.05 nm for the GS-1 soot. In general, soot oxidation is

https://doi.org/10.1021/acsomega.5c04848
ACS Omega 2025, 10, 50986−50994

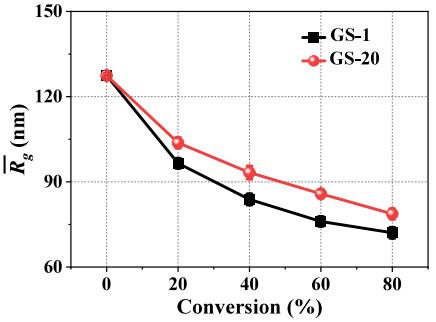

Figure 7. Averaged gyration radius values ($\overline{R_g}$) at different conversion levels.

accompanied by the fragmentation of soot aggregates,[31,32] and as a consequence, the aggregate size, in terms of $\overline{R_g}$, is decreased. It is also evident from Figure 7 that the GS-1 soot has smaller $\overline{R_g}$ values than the GS-20 soot at each conversion level. This difference in $\overline{R_g}$ is likely attributed to the much longer time for the GS-1 soot oxidation, as indicated in Figure 1, leading to a greater degree of fragmentation of the soot aggregates.

Figure 8 displays the D_f values of soot samples with different oxidized conversions. In the conversion range of interest, the

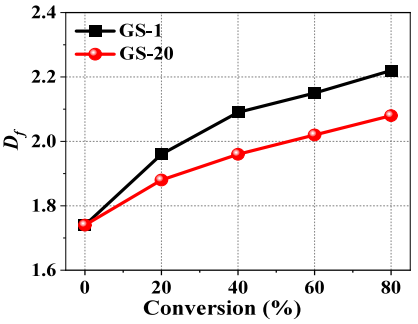

Figure 8. Fractal dimensions (D_f) at different conversion levels.

D_f increases from 1.74 to 2.22 for GS-1 soot and from 1.74 to 2.08 for GS-20 soot. In the case of soot particles, the aggregates with more chain-like cluster characteristics tend to possess smaller D_f values,[33−35] which are indicative of a lower degree of structural compactness. Because the low degree of structural compactness is typically associated with a large specific surface area and higher density of active sites for oxygen interaction, the aggregates having smaller D_f values are more vulnerable to complete oxidation. Hence, both soot samples display an increase in the D_f values with an increasing conversion level. At the same conversion level, the GS-20 soot has a smaller D_f than the GS-1 soot, likely because the high O_2 concentration favors the complete oxidation of the more compact aggregates in the GS-20 soot. Due to the fact that the compact aggregate structures are difficult to expose more active sites, the GS-1 soot particles generated at an oxygen-lean atmosphere have lower oxidative reactivity.[35,36]

3.3. Soot Nanostructure. To quantitatively characterize the changes of soot nanostructure under different oxygen atmospheres, the $\overline{L_f}$ and $\overline{T_f}$were calculated using HRTEM images. Figure 9 shows the values of $\overline{L_f}$ and $\overline{T_f}$ for the GS-1 and GS-20 soot samples during oxidation. By increasing the

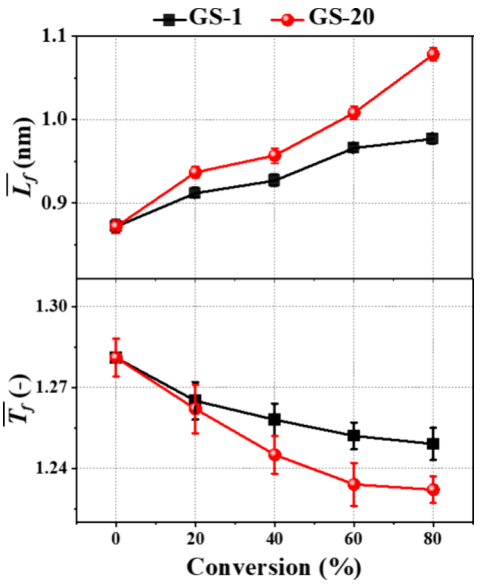

Figure 9. Averaged fringe length ($\overline{L_f}$) and tortuosity ($\overline{T_f}$) values of the soot samples at different conversion levels.

conversion from 0% to 80%, the $\overline{L_f}$ values increase from 0.822 to 1.028 nm for the GS-20 soot and from 0.822 to 0.927 nm for the GS-1 soot, while the $\overline{T_f}$ values marginally decrease from 1.281 to 1.232 for the GS-20 soot and from 1.281 to 1.249 for the GS-1 soot. These nanostructural changes suggest that both soot samples are transformed into more ordered structures with oxidation. The structural ordering observed during soot oxidation is generally attributed to crystallite growth and/or the selective oxidation of the disordered components in soot particles.[6,8] In general, the growth of crystallite occurs at temperatures exceeding 600 °C.[8,37] Since the oxidation temperature in this study was set at 500 °C, the structural ordering shown in Figure 9 can be attributed to the preferential oxidation of the disordered fraction. In addition, the GS-20 soot exhibits longer $\overline{L_f}$ but lower $\overline{T_f}$ compared to the GS-1 soot at the same conversion level, inferring that the high O_2 concentration enhances the preferential oxidation of the disordered fraction (shorter fringe length and higher tortuosity) in the soot particles.

3.4. Surface Functional Groups. *3.4.1. Aliphatic C−H Groups.* FT-IR spectroscopy was utilized to investigate the change in the aliphatic C−H groups on the soot surface. As an example, Figure 10 presents the FT-IR spectra of the GS-1 soot during oxidation. Drawing on the previous studies by

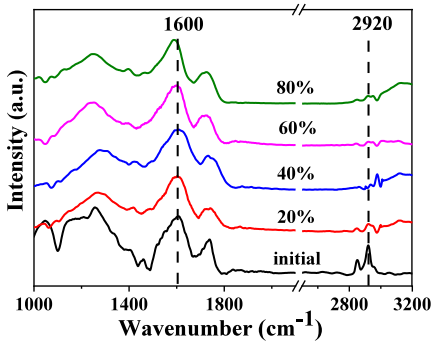

Figure 10. FT-IR spectra of the GS-1 soot during oxidation.

https://doi.org/10.1021/acsomega.5c04848
ACS Omega 2025, 10, 50986−50994

Santamaría et al.[38] and McKinnon et al.,[39] the relative concentrations of the aliphatic C−H groups on the soot surface can be represented by the ratio of the intensity of the aliphatic C−H peak at 2920 cm^{-1} to the aromatic C═C peak at 1620 cm^{-1} (I_{2925}/I_{1620}). It is well-known that soot particles primarily consist of amorphous and graphitic carbon. Because the more disordered structure of amorphous carbon involves a higher density of dangling bonds capable of producing C−H groups,[40,41] amorphous carbon possesses more aliphatic C−H groups than graphitic carbon. During the initial stage of soot oxidation, amorphous carbon is preferentially oxidized,[42−44] and so, the I_{2920}/I_{1620} ratios for both the GS-1 and GS-20 soot samples sharply decrease from 0.486 to 0.126 over the conversion range of 0−20%, as shown in Figure 11. With a

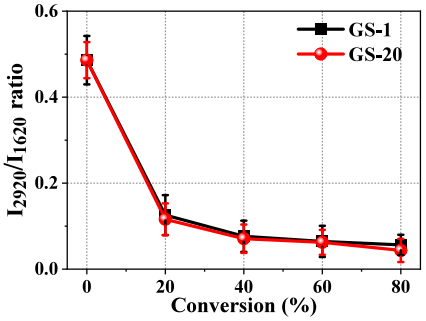

Figure 11. I_{2920}/I_{1620} ratios of the soot samples at different conversion levels.

further increase in the extent of conversion from 20 to 80%, the I_{2925}/I_{1620} ratios undergo a minimal decrease to approximately 0.050 due to the elimination of the graphitic carbon with fewer aliphatic C−H groups. Comparable findings were reported by Alfè et al.,[45] who observed that the H/C atomic ratio (which reflects the number of C−H groups) of the soot generated from premixed flames decreased in response to the increase in the degree of structural ordering. Furthermore, it is observed from Figure 11 that the GS-1 and GS-20 soot samples have almost equivalent I_{2925}/I_{1620} ratios during oxidation, indicating little effect of the concentration of O_2 on the number of aliphatic C−H groups.

3.4.2. Oxygenated Functional Group. XPS analysis was conducted to assess the oxygenated functional groups, including C−OH and C═O groups, of the soot samples. Following deconvolution of the C 1s spectra, the peak at 286.6 is assigned to C−OH, and the peak at 288.4 eV corresponds to C═O groups (see Figure 12).[46,47] The relative concentration of each oxygenated functional group is determined from the ratio of the corresponding peak relative to that of the C 1s peak.

Figure 13 shows the variation of the C−OH and C═O group concentrations during soot oxidation. There are high concentrations of oxygenated functional groups on the pristine soot. Because these oxygenated groups are highly reactive,[48,49] they are preferentially involved in soot oxidation and consumed in the early stage of the oxidation reaction. Thus, both the GS-1 and GS-20 soot samples display an abrupt decrease in the concentrations of these groups as the conversion decreases from 0 to 20%. As the oxidation proceeds, the contents of both the C−OH and C═O groups marginally decrease after an initial increase. Previous studies have indicated an increase in the specific surface area of soot

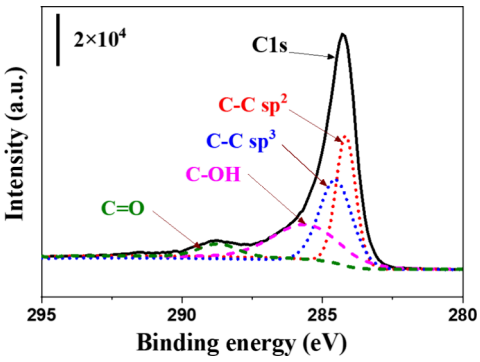

Figure 12. Typical XPS C 1s spectra after deconvolution for GS-20 soot at 40% conversion.

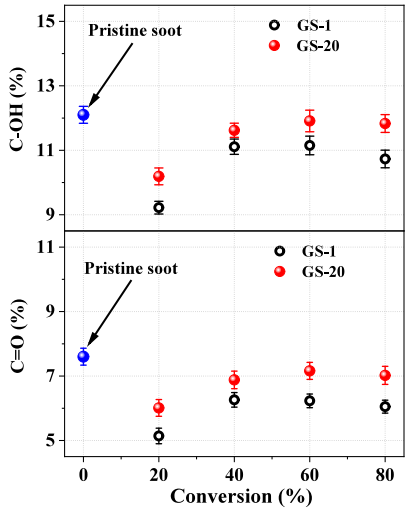

Figure 13. Concentrations of C−OH and C═O groups on the surfaces of the GS-1 and GS-20 soot samples at various conversion levels.

particles with oxidation. Ishiguro et al.[50] found that the specific surface area of a diesel exhaust soot was increased by a factor of 4.2 times after 50% of the soot had been oxidized in air. Similarly, Gilot et al.[51] reported that when 60% of carbon black Regal 600 had been oxidized in air, the specific surface area increased from 100 to 650 $m^2\ g^{-1}$. Both C−OH and C═O groups can be generated as intermediates when soot is oxidized by O_2.[52,53] A larger specific surface area provides additional active sites for oxygen interaction, leading to the formation of more C−OH and C═O groups on the soot surface. On the other hand, the structural ordering evidenced in Section 3.3 would be expected to decrease the oxidative reactivity of soot particles.[8,9,29] The low oxidative reactivity increases the resistance of soot particles to oxidation, resulting in the formation of fewer C−OH and C═O groups. As a result of the competition between the above two factors, the concentrations of C−OH and C═O groups in Figure 13 initially increase and then slightly decrease over the conversion range of 20−80%.

It is also obvious in Figure 13 that the GS-20 soot has higher concentrations of C−OH and C═O groups than the GS-1 soot at any given conversion level. This difference in functional group concentrations is attributed to the different O_2 concentrations provided for soot oxidation, with a higher O_2 concentration generating more such groups. Song et al.[13]

https://doi.org/10.1021/acsomega.5c04848
ACS Omega 2025, 10, 50986−50994

suggested that surface-oxygenated functional groups on soot particles can trigger oxidant attacks during oxidation. Thus, a higher concentration of these groups generally has a higher oxidative reactivity.

3.5. Carbon Chemical State. The carbon atoms in soot particles typically have two chemical states: sp^3 and sp^2 hybridizations.[40,46,54] In this work, XPS was used to obtain information concerning the hybridization in the soot samples. Following deconvolution of the high-resolution C 1s peak in Figure 12, the peaks at approximately 284.4 and 285.3 eV were determined to correspond to sp^2- and sp^3-hybridized carbon, respectively.[46,54] Thus, the hybridized carbon state of soot samples is characterized using the ratio of sp^2 peak area to sp^3 peak area.

Figure 14 shows the sp^2/sp^3 ratios for the GS-1 and GS-20 soot samples during oxidation. The sp^2/sp^3 ratios increase

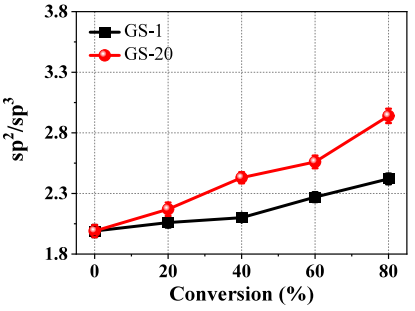

Figure 14. Ratios of sp^2/sp^3 for GS-1 and GS-20 soot samples during oxidation.

from 1.99 to 2.42 for the GS-1 soot and from 1.99 to 2.94 for the GS-20 soot with conversions from 0% up to 80%, indicative of an increase in the proportion of sp^2 carbon in the soot particles. The sp^2 hybridization state reflects the graphitic structure within the basal planes, while the sp^3 hybridization indicates the defect sites that interfere with the sp^2 hybridized network, reducing the material's long-range structural order.[43,44] Thus, the increase in the sp^2/sp^3 ratios suggests a transformation toward a more orderly graphitic structure, in agreement with the assessment of the soot nanostructure in Section 3.3. The increase in the sp^2/sp^3 ratio shown in Figure 14 is, of course, attributed to the preferential oxidation of the disordered fraction, as discussed above.

Compared with the GS-1 soot, the GS-20 soot exhibits a larger sp^2/sp^3 ratio at all conversion levels, as shown in Figure 14. Thus, the latter has a more ordered structure than the former, in keeping with the nanostructural results provided in Section 3.3. The larger sp^2/sp^3 ratio for the GS-20 soot can be attributed to the higher O_2 concentration, which promotes the preferential oxidation of the disordered fraction that contains more sp^3 carbon.

4. CONCLUSIONS

To clarify the differences in physicochemical properties and oxidative characteristics of GDI soot under oxygen-lean and oxygen-rich atmospheres, thermogravimetric analysis, HRTEM, XPS, and FT-IR were employed to investigate the specific oxidation rates (R_{sp}), primary particle size ($\overline{d}_p$), gyration radius (R_g), fractal dimension (D_f), surface functional group, hybridized carbon state, fringe length ($\overline{L}_f$), and tortuosity ($\overline{T}_f$) of GS-1 and GS-20 soot particles. The main conclusions can be summarized as follows:

First, at the same conversion level, the R_{sp} values for the GS-1 soot are 15 times lower than those of the GS-20 soot. Both GS-20 and GS-1 soot samples show an increase in the D_f and a decrease in the $\overline{d}_p$ and R_g by increasing the conversion level. In addition, both the soot samples undergo a gradual transformation into more ordered structures, as evidenced by an increase in the sp^2/sp^3 ratio, a decrease in $\overline{T}_f$, and an increase in the $\overline{L}_f$. These variations in the morphology and nanostructure increase the activation energy required for oxidation, making soot oxidation more challenging. Second, the oxygenated and aliphatic C−H groups on the surface of pristine soot are found to be preferentially involved in the oxidation process and are consumed in the early stages of the oxidation reaction. In addition, a certain number of oxygenated groups are generated on the surface of the soot during the oxidation process. Attributed to the oxygen-lean atmosphere, the surface of the GS-1 soot exhibits lower concentrations of C−OH and C═O groups than that of GS-20, hindering subsequent oxidation. Third, at the same conversion level, the GS-1 soot shows a smaller R_g, larger $\overline{d}_p$, and larger D_f than GS-20 in morphology and shorter $\overline{L}_f$ and higher $\overline{T}_f$ in its nanostructure. During passive regeneration of GPFs, the low oxygen concentration leads to a slower soot oxidation rate and results in the formation of more compact soot agglomerates, which increases the difficulty of oxidation. To improve the efficiency of passive regeneration, a catalyst coating was applied to promote oxidation. In addition, the residual soot from passive regeneration exhibits a relatively disordered nanostructure, which provides certain advantages when active regeneration is carried out with an increased oxygen concentration.

AUTHOR INFORMATION

Corresponding Author

Chonglin Song − *State Key Laboratory of Engines, Tianjin University, Tianjin 300072, China;* orcid.org/0009-0009-8279-0037; Email: 2016201275@tju.edu.cn

Authors

Chenxi Wang − *State Key Laboratory of Engines, Tianjin University, Tianjin 300072, China; Institute for Transport Studies, University of Leeds, Leeds LS2 9JT, U.K.;* orcid.org/0009-0001-4840-5854

Xiangyu Dong − *State Key Laboratory of Engines, Tianjin University, Tianjin 300072, China*

Ye Liu − *State Key Laboratory of Engines, Tianjin University, Tianjin 300072, China; Institute for Transport Studies, University of Leeds, Leeds LS2 9JT, U.K.*

Xuyang Zhang − *State Key Laboratory of Engines, Tianjin University, Tianjin 300072, China*

Gang lv − *State Key Laboratory of Engines, Tianjin University, Tianjin 300072, China*

Complete contact information is available at: https://pubs.acs.org/10.1021/acsomega.5c04848

Author Contributions

C.W.: conceptualization, methodology, investigation, formal analysis, data curation, visualization, and writing—original draft. X.D.: resources, methodology, investigation, and data curation. X.Z.: resources, methodology, investigation, and data

https://doi.org/10.1021/acsomega.5c04848
ACS Omega 2025, 10, 50986−50994

curation. G.L.: funding acquisition, investigation, and data curation. Y.L.: resources and data curation. C.S.: conceptualization, investigation, project administration, resources, funding acquisition, supervision, and writing—reviewing and editing.

Notes

The authors declare no competing financial interest.

■ ACKNOWLEDGMENTS

This study was supported by the National Natural Science Foundation of China (No. 52176123).

■ REFERENCES

(1) Martínez-Munuera, J. C.; Zoccoli, M.; Giménez-Mañogil, J.; García-García, A. Lattice oxygen activity in ceria-praseodymia mixed oxides for soot oxidation in catalysed gasoline particle filters. *Applied Catalysis B: Environmental* **2019**, *245*, 706−720.

(2) Wong, P. K.; Ghadikolaei, M. A.; Chen, S. H.; et al. Physical, chemical, and cell toxicity properties of mature/aged particulate matter (PM) trapped in a diesel particulate filter (DPF) along with the results from freshly produced PM of a diesel engine. *Journal of Hazardous Materials* **2022**, *434*, No. 128855.

(3) Boger, T.; Rose, D.; Nicolin, P.; Gunasekaran, N.; Glasson, T. Oxidation of soot (Printex® U) in particulate filters operated on gasoline engines. *Emission Control Science and Technology* **2015**, *1* (1), 49−63.

(4) Ge, H.; Ye, Z.; He, R. Raman spectroscopy of diesel and gasoline engine-out soot using different laser power. *Journal of Environmental Sciences* **2019**, *79*, 74−80.

(5) Boger, T.; Rose, D.; Nicolin, P.; Coulet, B.; Bachurina, A. Severe soot oxidations in gasoline particulate filter applications. *SAE Technical Paper Series, 2018-01-1699*.

(6) Al-Qurashi, K.; Boehman, A. L. Impact of exhaust gas recirculation (EGR) on the oxidative reactivity of diesel engine soot. *Combust. Flame* **2008**, *155*, 675−695.

(7) Zhang, Z.; Balasubramanian, R. Physicochemical and toxicological characteristics of particulate matter emitted from a non-road diesel engine: Comparative evaluation of biodiesel-diesel and butanol-diesel blends. *Journal of Hazardous Materials* **2014**, *264*, 395−402.

(8) Huang, J.; Gao, J.; Gao, J.; Huang, Y.; Wang, X.; Wang, S.; Qi, M.; Tian, G. Insight into the mechanism of solution organic fractions on soot oxidation activity enhancement. *J. Hazard. Mater.* **2024**, *479*, No. 135606.

(9) Vander Wal, R. L.; Tomasek, A. J. Soot oxidation: dependence upon initial nanostructure. *Combust. Flame* **2003**, *134*, 1−9.

(10) Guo, X.; Zheng, Q.; Zhou, C.; et al. Assessment of the effect of dimethyl carbonate on regulated/ unregulated emissions, polycyclic aromatic hydrocarbons and soot particles. *Process Safety and Environmental Protection* **2024**, *184*, 445−461.

(11) Wei, J.; Lu, W.; Zeng, Y.; et al. Physicochemical properties and oxidation reactivity of exhaust soot from a modern diesel engine: Effect of oxyfuel type. *Combust. Flame* **2022**, *238*, No. 111940.

(12) Pan, M.; Wang, Y.; Wei, J.; et al. Impact of carbon chain length of alcohols on the physicochemical properties and reactivity of exhaust soot. *Science of The Total Environment* **2021**, *799*, No. 149434.

(13) Song, J.; Alam, M.; Boehman, A. L.; Kim, U. Examination of the oxidation behavior of biodiesel soot. *Combust. Flame* **2006**, *146*, 589−604.

(14) Setiabudi, A.; Makkee, M.; Moulijn, J. A. The role of NO_2 and O_2 in the accelerated combustion of soot in diesel exhaust gases. *Applied Catalysis B: Environmental* **2004**, *50*, 185−194.

(15) Wang, X.; Chen, W.; Huang, Y.; Wang, L.; Zhao, Y.; Gao, J. Advances in soot particles from gasoline direct injection engines: A focus on physical and chemical characterization. *Chemosphere* **2023**, *311*, No. 137181.

(16) Wu, Z.; Song, C.; Lv, G.; Pan, S.; Li, H. Morphology, fractal dimension, size and nanostructure of exhaust particles from a spark-ignition direct-injection engine operating at different air−fuel ratios. *Fuel* **2016**, *185*, 709−717.

(17) Vishal, V.; Mallikarjuna, J. M. Effect of engine parameters on the mixture distribution, performance and emission characteristics of a gasoline direct injection engine with baffles-A numerical analysis. *Energy* **2024**, *312*, No. 133543.

(18) Rubino, L.; Their, D.; Schumann, T.; Guettler, S.; Russ, G. Fundamental study of GPF performance on soot and ash accumulation over artemis urban and motorway cycles comparison of engine bench results with GPF durability study on road. *SAE Technical Paper, 2017-24-0127*.

(19) Zhang, X. Y.; Song, C. L.; Lyu, G.; Li, Y. Q.; Qiao, Y. H.; Li, Z. G. Physicochemical analysis of the exhaust soot from a gasoline direct injection (GDI) engine and the carbon black. *Fuel* **2022**, *322*, No. 124262.

(20) Jang, J.; Lee, J.; Choi, Y.; Park, S. Reduction of particle emissions from gasoline vehicles with direct fuel injection systems using a gasoline particulate filter. *Sci. Total Environ.* **2018**, *644*, 1418−1428.

(21) Shimoda, T.; Ito, Y.; Saito, C.; Nakatani, T.; Shibagaki, Y.; Yuuki, K.; Sakamoto, H.; Vogt, C.; Matsumoto, T.; Furuta, Y.; Heuss, W.; Kattouah, P.; Makino, M. Potential of a Low Pressure Drop Filter Concept for Direct Injection Gasoline Engines to Reduce Particulate Number Emission. *SAE Technical paper, 2012-01-1241*.

(22) Yehliu, K.; Vander Wal, R. L.; Boehman, A. L. Development of an HRTEM image analysis method to quantify carbon nanostructure. *Combust. Flame* **2011**, *158*, 1837−1851.

(23) Saffaripour, M.; Chan, T. W.; Liu, F. S.; Thomson, K. A.; Smallwood, G. J.; Kubsh, J.; Brezny, R. Effect of drive cycle and gasoline particulate filter on the size and morphology of soot particles emitted from a gasoline-direct-Injection vehicle. *Environmental Science & Technology*. **2015**, *49*, 11950−11958.

(24) Neer, A.; Koylu, U. O. Effect of operating conditions on the size, morphology, and concentration of submicrometer particulates emitted from a diesel engine. *Combust. Flame* **2006**, *146*, 142−154.

(25) Lee, K. O.; Cole, R.; Sekar, R.; Choi, M. Y.; Kang, J. S.; Bae, C. S.; Shin, H. D. Morphological investigation of the microstructure, dimensions, and fractal geometry of diesel particulates. *Proceedings of the Combustion Institute* **2002**, *29* (1), 647−653.

(26) Verma, P.; Pickering, E.; Jafari, M.; Guo, Y.; Stevanovic, S.; Fernando, J. F. S.; Golberg, D.; Brooks, P.; Brown, R.; Ristovski, Z. Influence of fuel-oxygen content on morphology and nanostructure of soot particles. *Combust. Flame* **2019**, *205*, 206−219.

(27) Megaridis, C. M.; Dobbins, R. A. Morphological description of flame-generated materials. *Combust. Sci. Technol.* **1990**, *71*, 95−109.

(28) Seon, H.; Choi, S. Oxidation-derived maturing process of soot, dependent on O_2-NO_2 mixtures and temperatures. *Carbon* **2015**, *93*, 1068−1076.

(29) Liu, Y.; Zhang, X. Y.; Lyu, G.; Qiao, Y. H.; Zhang, W.; Song, C. L. Effect of the oxidation-induced fragmentation of primary particles on soot oxidation reactivity. *Combust. Flame* **2022**, *240*, No. 112026.

(30) Lapuerta, M.; Oliva, F.; Agudelo, J.; Boehman, A. L. Effect of fuel on the soot nanostructure and consequences on loading and regeneration of diesel particulate filters. *Combust. Flame* **2012**, *159* (2), 844−853.

(31) Ghiassi, H.; Toth, P.; Jaramill, I. C.; Lighty, J. S. Soot oxidation-induced fragmentation: Part1: The relationship between soot nanostructure and oxidation-induced fragmentation. *Combust. Flame* **2016**, *163*, 179−187.

(32) Ghiassi, H.; Jaramill, I. C.; Toth, P.; Lighty, J. S. Soot oxidation-induced fragmentation: Part 2: Experimental investigation of the mechanism of fragmentation. *Combust. Flame* **2016**, *163*, 170−178.

(33) Lee, K. O.; Cole, R.; Sekar, R.; Choi, M. Y.; Kan, J. S.; Bae, C. S.; Shin, H. D. Morphological investigation of the microstructure, dimensions, and fractal geometry of diesel particulates. *Proc. Combust. Inst.* **2002**, *29* (1), 647−653.

(34) Meakin, P.; Stanley, H. E.; Ostrowsky, N. Computer Simulation of Growth and Aggregation Processes. *On Growth and Form* **1986**, 111−135.

https://doi.org/10.1021/acsomega.5c04848
ACS Omega 2025, 10, 50986−50994

(35) Zhang, R. L.; Zhang, Y. L.; Kook, S. H. Morphological variations of in-flame and exhaust soot particles associated with jet-to-jet variations and jet-jet interactions in a light-duty diesel engine. *Combust. Flame* **2017**, *176*, 377−390.
(36) Zhang, Y.; Kim, D.; Rao, L.; Kook, S.; Kim, K. S.; Kweon, C. B. In-flame soot particle structure on the up- and down-swirl side of a wall-interacting jet in a small-bore diesel engine. *Proceedings of the Combustion Institute* **2019**, *37* (4), 4847−4855.
(37) Fang, H. L.; Lance, M. J. Influence of Soot Surface Changes on DPF Regeneration. *SAE Technical paper, 2004-01-3043*.
(38) Santamaría, A.; Mondragón, F.; Molina, A.; Marsh, N. D.; Eddings, E. G.; Sarofim, A. F. FTIR and ^{1}H NMR characterization of the products of an ethylene inverse diffusion flame. *Combust. Flame* **2006**, *146*, 52−62.
(39) McKinnon, J. T.; Meyer, E.; Howard, J. B. Infrared analysis of flame-generated PAH samples. *Combust. Flame* **1996**, *105* (1−2), 161−166.
(40) Azevedo, A. F.; Matsushima, J. T.; Vicentin, F. C.; Baldan, M. R.; Ferreira, N. G. Surface characterization of NCD films as a function of sp^2/sp^3 carbon and oxygen content. *Appl. Surf. Sci.* **2009**, *255*, 6565−6570.
(41) Sun, C. X.; Martin, J.; Boehman, A. L. Nanostructure and reactivity of soot produced from a turbodiesel engine using post injection. *Proceedings of the Combustion Institute* **2019**, *37* (1), 1169−1176.
(42) Knauer, M.; Carrara, M.; Rothe, D.; Niessner, R.; Ivleva, N. P. Changes in Structure and Reactivity of Soot during Oxidation and Gasification by Oxygen, Studied by Micro-Raman Spectroscopy and Temperature Programmed Oxidation. *Aerosol Sci. Technol.* **2009**, *43* (1), 1−8.
(43) Knauer, M.; Schuster, M. E.; Su, D.; Schlogl, R.; Niessner, R.; Ivleva, N. P. Soot structure and reactivity analysis by Raman microspectroscopy, temperature-programmed oxidation, and high-resolution transmission electron microscopy. *J. Phys. Chem. A* **2009**, *113*, 13871−13880.
(44) Qiao, Y. H.; Wang, C. X.; Lyu, G.; Jing, Z. M.; Li, Y. Q.; Song, C. L. Understanding the oxidation kinetics of diesel exhaust soot during oxidation process. *Chemosphere* **2023**, *311*, No. 136980.
(45) Alfè, M.; Apicella, B.; Barbella, R.; Rouzaud, J. N.; Tregrossi, A.; Ciajolo, A. Structure−property relationship in nanostructures of young and mature soot in premixed flames. *Proceedings of the Combustion Institute* **2009**, *32*, 697−704.
(46) Vander Wal, R. L.; Bryg, V. M.; Hays, M. D. XPS analysis of combustion aerosols for chemical composition, surface chemistry, and carbon chemical state. *Anal. Chem.* **2011**, *83* (6), 1924−1930.
(47) Vander Wal, R. L.; Bryg, V. M.; Hays, M. D. Fingerprinting soot (towards source identification): physical structure and chemical composition. *J. Aerosol Sci.* **2010**, *41*, 108−117.
(48) Song, J.; Alam, M.; Boehman, A. L. Impact of alternative fuels on soot properties and DPF regeneration. *Combust. Sci. Technol.* **2007**, *179* (9), 1991−2037.
(49) Levi, G.; Senneca, O.; Causà, M.; Salatino, P.; Lacovig, P.; Lizzit, S. Probing the chemical nature of surface oxides during coal char oxidation by high-resolution XPS. *Carbon* **2015**, *90*, 181−196.
(50) Ishiguro, T.; Suzuki, N.; Fujitani, Y.; Morimoto, H. Microstructural changes of diesel soot during oxidation. *Combust. Flame* **1991**, *85* (1−2), 1−6.
(51) Gilot, P.; Bonnefoy, F.; Marcuccilli, F.; Prado, G. Determination of kinetic data for soot oxidation. Modeling of competition between oxygen diffusion and reaction during thermogravimetric analysis. *Combust. Flame* **1993**, *95*, 87−100.
(52) Raj, A.; Yang, S. Y.; Cha, D.; Tayouo, R.; Chung, S. H. Structural effects on the oxidation of soot particles by O_2: Experimental and theoretical study. *Combust. Flame* **2013**, *160* (9), 1812−1826.
(53) Williams, S. Surface intermediates, mechanism, and reactivity of soot oxidation. Ph.D. thesis, University of Toronto: Toronto, 2008.
(54) Garcia, X.; Soler, L.; Casanovas, A.; Escudero, C.; Llorca, J. X-ray photoelectron and Raman spectroscopy of nanostructured ceria in soot oxidation under operando conditions. *Carbon* **2021**, *178*, 164−180.

https://doi.org/10.1021/acsomega.5c04848
ACS Omega 2025, 10, 50986−50994